INTERNATIONAL JOURNAL FOR NUMERICAL METHODS IN FLUIDS
Int. J. Numer. Meth. Fluids 2006; **51**:849–879
Published online 28 December 2005 in Wiley InterScience (www.interscience.wiley.com). DOI: 10.1002/fld.1149

A numerical study of fully developed laminar flows in pipes with two planar curvatures

C. Niewiadomski[1,‡], M. Paraschivoiu[2,*,†] and P. Sullivan[1,§]

[1]*Department of Mechanical and Industrial Engineering, University of Toronto, Canada*
[2]*Department of Mechanical and Industrial Engineering, Concordia University, Canada*

SUMMARY

The spectral element method is applied on unstructured tetrahedral elements to solve the Navier–Stokes equations for fully developed laminar flow in pipes with two planar curvatures. Specific implementations of the spectral element method to double curved pipes and parallelization are described. Previous studies on flows in pipes focused on constant curvature or torsion geometries, as well as pipes with varying curvature. This study focuses on the periodic variation of both the curvature as well as torsion by analysing a pipe having two planar curvatures. The effects of the three parameters defining the pipe are studied to isolate the curvature and torsion effect on the magnitude and angle of the secondary flow. Furthermore, the geometric effects on the wall shear stress are studied, as it is an important fluid flow property, especially in blood flows. Copyright © 2006 John Wiley & Sons, Ltd.

KEY WORDS: spectral element method; Navier–Stokes equations; wall shear stress

1. INTRODUCTION

A pipe geometry can be defined by the curvature and torsion of its centreline as well as by the cross-sectional profile. The effects of the cross-sectional profiles are well understood and studied. Nevertheless the curvature of a pipe induces a secondary flow which was first studied by Dean [1] using a perturbation solution. This fluid phenomenon is explained through an

*Correspondence to: M. Paraschivoiu, Concordia University, 1455 de Maisonneuve Blvd West Montreal, Quebec, Canada H3G 1H8.
†E-mail: paraschi@me.concordia.ca
‡E-mail: niewiac@mie.utoronto.ca
§E-mail: pierre.sullivan@utoronto.ca

Contract/grant sponsor: Natural Sciences and Engineering Research Council of Canada
Contract/grant sponsor: Joseph Bazylewicz Fellowship

Received 28 September 2004
Revised 1 November 2005
Accepted 3 November 2005

imbalance of the axial pressure gradient and the centrifugal force, leading to a formation of a secondary flow. This secondary flow is characterized by the movement of the fluid in the middle toward the outer wall. This fluid impinges on the outer wall and is forced to turn and move down along the wall to merge at the inner wall. Fluid flow in curved pipes is found widely in industrial applications such as: heat exchangers, fluid transport and mixing as well as power generation, moreover it is found in biological applications such as blood and air flow. Curved pipes, implying constant curvature, have been reviewed extensively by Berger [2] and Ito [3]. Most of the studies up to that point focused on pipes with small curvature ratios $\kappa = D/R_k$, where D is the diameter of the pipe and R_k is the radius of curvature. These laminar flows are only influenced by the Dean number $De = Re\sqrt{\kappa}$ and the inlet flow conditions, where Re is the Reynolds number and κ is the curvature ratio. The Dean number quantifies the ratio of a square root of the product of inertial and centrifugal forces to the viscous forces. Although these flows are well understood, high Dean number flows present specific challenges, such as multiple laminar solutions found by Yang [4]. Helical pipes were studied by Germano [5, 6], Wang [7], Murata [8] and Yamamoto [9] to detail the torsion effect on the flow. Helical pipes can be defined by a constant curvature and torsion, allowing to study these two effects separately. Some of these researchers expanded the second-order perturbation solution into the helical coordinate system. However, these perturbation solutions are only valid for small curvature ratios. This restriction has been overcome by other authors through seeking a numerical solution, mostly employing the Finite Difference and Finite Volume methods. It was found that the flow in helical pipes is governed by the Dean number De as well as a new non-dimensional variable Gn the Germano number. The Germano number quantifies the ratio of the twisting to the viscous forces, $Gn = Re\,\tau$, where τ is the torsion. Nevertheless most pipes found in nature cannot be defined simply by constant curvature and torsion. To address this, flows with changing curvatures were studied by Itmoto [10] and recently by Yang [11], especially for applications in solar heat exchangers which have periodically varying curvature. Although most of his studies were focused on heat transfer, the author noticed an increasing pressure drop with increasing curvature for a given flow rate. Despite this, no studies up to this point were performed on flows with both the variation of curvature and torsion, representing naturally occurring pipes. This study focuses on such flows where both the torsion and the curvature are varied periodically. A model pipe is constructed possessing two planar radii of curvature, representing an arbitrarily curved and torsioned pipe. The effects of changing curvature and torsion are studied through varying the three parameters describing the model pipe. To capture this complex geometry and obtain highly accurate solutions, the spectral element method with curved elements, which is an expansion of the Finite Element Method (FEM), is employed. Details of the spectral element method implementation are also presented.

Firstly, this paper introduces the basic governing equations and a solution strategy based on the splitting method. Secondly the spectral element method is summarized and specific implementation to double curved pipes as well as challenges in simple higher order post-processing are explained. Validation results for the spectral element method of both a manufactured solution and a curved pipe are presented. Next the model pipe geometry construction process is described followed by the results for the variation of the respective radii and number of periodic periods. Finally, the effects of the geometry on the wall shear stress are described.

2. GOVERNING EQUATIONS

The main focus of this paper is to study complex flows, such as the flows in pipes with two curvatures, by solving the unsteady incompressible Navier–Stokes equations, which govern the behaviour of a Newtonian fluid. The Reynolds number is defined as $Re = UL/v$, where U is a characteristic velocity, L is a characteristic length and v is the kinematic viscosity of the fluid. These equations are written in the vector form as

$$\frac{\partial \mathbf{u}}{\partial t} + \mathbf{u} \cdot \bigtriangledown \mathbf{u} = -\bigtriangledown p + \frac{1}{Re} \bigtriangledown^2 \mathbf{u} \quad \text{in } \Omega$$

$$\bigtriangledown \cdot \mathbf{u} = 0 \quad \text{in } \Omega$$

where $\mathbf{u}$ is the velocity vector and p is the pressure field. In order to solve these equations, boundary and initial conditions need to be applied which can be written as

$$\mathbf{u} = u_{\mathrm{D}} \quad \text{on } \partial\Omega_{\mathrm{D}}$$

$$\mathbf{u}(\mathbf{x}, 0) = \mathbf{u}^{\mathbf{0}}(\mathbf{x})$$

where for simplicity, only Dirichlet domain boundary ($\partial\Omega_{\mathrm{D}}$) is considered.

3. SOLUTION STRATEGY

The spectral element method is a subset of the method of weighted residuals. Therefore, the weak formulation of Navier–Stokes equations is reviewed. The appropriate space for the pressure is chosen to be square integrable $L^2 = \{f \in \Re^3 | \int f^2 \, \mathrm{d}\Omega < \infty\}$ over Ω, with the integral over the domain being zero, i.e., $L_0^2(\Omega) = \{q \in L^2 | \int_\Omega q \, \mathrm{d}\Omega = 0\}$. Moreover, for each velocity component a space of functions v is required such that $v \in [L^2(\Omega)]$ and $\bigtriangledown v \in [L^2(\Omega)]$, which is denoted by $H_0^1(\Omega)$ and includes the Dirichlet boundary conditions. The weak formulation of the Navier–Stokes equations becomes, find $\mathbf{u} \in [H_0^1(\Omega)]^3$ and $p \in [L_0^2(\Omega)]$ such that

$$\left(\mathbf{v}, \frac{\partial \mathbf{u}}{\partial t}\right) + (\mathbf{v}, \mathbf{u} \cdot \bigtriangledown \mathbf{u}) + \frac{1}{Re}(\bigtriangledown \mathbf{v}, \bigtriangledown \mathbf{u}) + (\mathbf{v}, \bigtriangledown p) = (\mathbf{v}, \mathbf{f}) \quad \forall \mathbf{v} \in [H_0^1(\Omega)]^3$$

$$(\bigtriangledown \cdot \mathbf{u}, q) = 0 \quad \forall q \in [L_0^2(\Omega)]$$

where the brackets indicate an integral of the internal product over the domain, $\mathbf{v}$ are the test functions for velocity and q are the test functions for pressure. Similar to the FEM the spectral element method subdivides the domain into a finite number of non-overlapping tetrahedral elements

$$\Omega = \bigcup_{e=1}^{N_{\mathrm{el}}} \Omega^e \quad \text{where} \quad \bigcap_{e=1}^{N_{\mathrm{el}}} \Omega^e = \emptyset$$

Furthermore, the bases are defined in each element such that the summation of all the bases over all elements with their respective coefficients describes the approximate solution: $u^\delta = \sum_{i=1}^{N_{\mathrm{dof}}} \hat{u}_i \phi_i$ as well as the trial function $\mathbf{v}$. In the Galerkin method the trial functions as well

as the base functions are the same. The Navier–Stokes equations are discretized temporally through a second-order implicit scheme such that the matrix formulation becomes

$$\left(\frac{3}{2}\frac{1}{\triangle t}\mathbf{M}+\frac{1}{Re}\mathbf{A}\right)\hat{\mathbf{u}}^{n+1}=\mathbf{F}^{n+1}+\mathbf{C}^{n+1}(\hat{\mathbf{u}})+\mathbf{M}\frac{1}{\triangle t}\left(2\hat{\mathbf{u}}^{n}-\frac{1}{2}\hat{\mathbf{u}}^{n-1}\right)+\mathscr{D}_p\hat{p}^{n+1}$$

$$\mathscr{D}_u\hat{\mathbf{u}}^{n+1}=0$$

where $\mathbf{A}$ is the stiffness matrix, $\mathbf{M}$ is the mass matrix, $\mathscr{D}_p$ is the derivative matrix, $\mathbf{F}^{n+1}$ contains the forcing term and boundary inhomogeneity. These matrices are constructed in the next section. The convection operator $\mathbf{C}^{n+1}(\hat{\mathbf{u}})$ is discretized through an explicit third-order multi-step scheme defined by Cardenas [12] such that

$$\mathbf{C}_j^{n+1}(\hat{\mathbf{u}}^n,\hat{\mathbf{u}}^{n-1},\hat{\mathbf{u}}^{n-2})=\tfrac{8}{3}\mathbf{B}^{\mathrm{T}}\mathbf{W}(\mathbf{B}\hat{\mathbf{u}}_i^n)(D_i\mathbf{B}\hat{\mathbf{u}}_j^n)-\tfrac{7}{3}\mathbf{B}^{\mathrm{T}}\mathbf{W}(\mathbf{B}\hat{\mathbf{u}}_i^{n-1})(D_i\mathbf{B}\hat{\mathbf{u}}_j^{n-1})$$

$$+\tfrac{2}{3}\mathbf{B}^{\mathrm{T}}\mathbf{W}(\mathbf{B}\hat{\mathbf{u}}_i^{n-2})(D_i\mathbf{B}\hat{\mathbf{u}}_j^{n-2})$$

where the matrices $\mathbf{B}$ and D_i as well as the $\mathbf{W}$ vector are defined in the next section. The derivatives are calculated using the precalculated derivatives of the bases. To exclude parasitic pressure modes a $\mathscr{P}_p/\mathscr{P}_{p-2}$ formulation introduced by Bernardi [13] is used, i.e., the pressure expansion is two orders lower than the velocity expansion. The splitting method reviewed by Fischer [14] is used to decouple the pressure by solving for a intermediate velocity, while ensuring divergence free flow such that

$$\mathbf{H}\tilde{\mathbf{u}}=\mathbf{F}^{n+1}+\mathbf{C}^{n+1}(\hat{\mathbf{u}})+\mathbf{M}\frac{1}{\triangle t}\left(2\hat{\mathbf{u}}^{n}-\frac{1}{2}\hat{\mathbf{u}}^{n-1}\right)+\mathscr{D}_p\hat{p}^{n}$$

$$\mathscr{A}_p\tilde{p}=-\frac{3}{2\triangle t}\mathscr{D}_u\tilde{\mathbf{u}}$$

$$\hat{\mathbf{u}}^{n+1}=\tilde{\mathbf{u}}+\frac{2\triangle t}{3}\mathbf{M}^{-1}\mathscr{D}_p\tilde{p}$$

$$\hat{p}^{n+1}=\hat{p}^{n}+\tilde{p}$$

where the Helmholtz matrix is defined as $\mathbf{H}=(\frac{3}{2}(1/\triangle t)\mathbf{M}+(1/Re)\mathbf{A})$ and $\mathscr{A}_p$ is the stiffness matrix of the pressure bases. The resulting pressure correction term $\tilde{p}$ is used to correct the velocity and the pressure at the succeeding timestep.

4. SPECTRAL ELEMENT METHOD

The spectral element method on unstructured meshes developed by Sherwin and Karniadakis [15, 16] is reviewed here as an expansion of the finite element method. A new coordinate system is introduced based on the hexahedral coordinate system. This coordinate system facilitates the elemental operations such as integration as well as formation of the bases. Two out of the three coordinate systems are equivalent to the FEM: the physical and reference coordinates, while the third system is called a collapsed coordinate system and is denoted

by η_1, η_2, η_3. The latter system is mapped onto the reference coordinate system in three steps: collapsing the top face of the hexahedron onto a line, collapsing the new line onto a vertex, and finally collapsing the square base onto a triangle. This transformation is summarized as

$$\eta_1 = \frac{4(1+\xi_1)}{(1-\xi_2)(1-\xi_3)}, \quad \eta_2 = \frac{2(1+\xi_2)}{(1-\xi_3)}, \quad \eta_3 = \xi_3$$

where ξ_1, ξ_2, ξ_3 denotes the reference coordinate system. It is seen that this mapping is singular at the points $\xi_2 = 1$ and $\xi_3 = 1$, which are the vertices C and D, respectively. Conversely the vertices A and B are defined on the base of the tetrahedron such that $\xi_3 = -1$ and $\xi_2 = -1$, while ξ_1 is -1 and 1, respectively. The mapping from the reference coordinate system to the physical system is identical to standard FEM being based on linear connection of the vertices. The bases are a subset of the modal hexahedral expansions, where certain faces and edges of the full hexahedral expansion are chosen and collapsed onto a tetrahedron. These bases are classified as: vertex, edge, face and interior modes. A vertex mode is a linear function defined as being one at its vertex and zero at the other vertices. Edge modes are defined as functions ranging from quadratic to order p, which are defined on its edge and are zero on the other edges. Face modes are defined as functions ranging from quadratic to order $p-1$, which are defined at its face and zero on the other faces. Finally an interior mode is defined only in the interior of the element and is zero on the boundaries. Jacobi polynomials are used to form the bases, as they are orthogonal in the integral inner product with respect to $(1-x)^{\alpha}(1+x)^{\beta}$ and can be formed through a recursive relation. Elemental operations need to be modified in order to use the new bases which are defined on the collapsed coordinate system. The first main elemental operation is the integration, it is performed on the reference coordinate system equivalent to the FEM such that it becomes

$$\begin{aligned}
\int_{\Omega_{\text{ref}}} u \partial\Omega_{\text{ref}} &= \int_{-1}^{1}\int_{-1}^{1}\int_{-1}^{1} u(\eta_1,\eta_2,\eta_3)\mathbf{J}_{\xi\to\eta}\partial\eta_1\,\partial\eta_2\,\partial\eta_3 \\
&= \int_{-1}^{1}\int_{-1}^{1}\int_{-1}^{1} u(\eta_1,\eta_2,\eta_3)\left(\frac{1-\eta_2}{2}\right)\left(\frac{1-\eta_3}{2}\right)^2 \partial\eta_1\,\partial\eta_2\,\partial\eta_3 \\
&= \sum_{i}^{Q_{\text{GLL}}}\sum_{j}^{Q_{\text{GRL}}}\sum_{k}^{Q_{\text{GRL}}} u(\eta_{1i}^{0,0},\eta_{2j}^{1,0},\eta_{3k}^{2,0}) w_i^{0,0}\,\hat{w}_j^{1,0}\,\hat{w}_k^{2,0}
\end{aligned}$$

$$\hat{w}_j^{1,0} = \frac{w_j^{1,0}}{2} \quad \hat{w}_k^{2,0} = \frac{w_k^{2,0}}{4}$$

where the Jacobian between the reference and collapsed coordinate system is included into the weights by modifying the Jacobi constant α and β. The quadrature points are the roots of the Jacobi polynomial $P_N^{\alpha,\beta}$ of order N. In the η_1 direction, a Gauss–Labatto–Jacobi quadrature point distribution is used which includes both the endpoints -1 and 1. However, the coordinates η_2 and η_3 exhibit a singularity at the point $\eta_2, \eta_3 = 1$. Therefore, Gauss–Radau–Jacobi quadrature point distribution is used in these directions as this distribution does not include the endpoint at 1, and avoids the evaluation of the singular vertices. The next main elemental operation is the differentiation. It is known that in the physical coordinate system the bases can be represented through Lagrange polynomials (h_p) and thus collocation differentiation can

be used. The differentiation is performed in the reference coordinate system equivalent to the FEM method such that it is first performed in the collapsed coordinate system as

$$\frac{\partial u}{\partial \eta_1}(\eta_1^{\mathrm{GLJ}}, \eta_2^{\mathrm{GRJ}}, \eta_3^{\mathrm{GRJ}}) = \sum_i^Q u_{pqr}^{\delta}(\eta_1^{\mathrm{GLJ}}, \eta_2^{\mathrm{GRJ}}, \eta_3^{\mathrm{GRJ}}) \frac{\partial h_p(\eta_{1i}^{\mathrm{GLJ}})}{\partial \eta_1} \delta(\eta_{2i}^{\mathrm{GRJ}})_q \delta(\eta_{3i}^{\mathrm{GRJ}})_r = D_{\eta_1} \mathbf{B}\hat{u}$$

and then is transformed onto the reference system through the chain rule

$$\begin{pmatrix} \dfrac{\partial}{\partial \xi_1} \\ \dfrac{\partial}{\partial \xi_2} \\ \dfrac{\partial}{\partial \xi_3} \end{pmatrix} = \begin{pmatrix} \dfrac{4}{(1-\eta_2)(1-\eta_1)} \dfrac{\partial}{\partial \eta_1} \\ \dfrac{2(1+\eta_1)}{(1-\eta_2)(1-\eta_3)} \dfrac{\partial}{\partial \eta_1} + \dfrac{2}{(1-\eta_3)} \dfrac{\partial}{\partial \eta_2} \\ \dfrac{2(1+\eta_1)}{(1-\eta_2)(1-\eta_3)} \dfrac{\partial}{\partial \eta_1} + \dfrac{(1+\eta_2)}{(1-\eta_3)} \dfrac{\partial}{\partial \eta_2} + \dfrac{\partial}{\partial \eta_3} \end{pmatrix}$$

to be treated as in the FEM. A specific implementation of the derivative treatment which combines precalculation of the derivatives of the bases and the tensor-product factorization is explained in Section 5.3.

Having defined the elemental operations, the basic elemental matrices are introduced. Firstly, the mass matrix is an inner product of the bases defined as: $\mathbf{M} = (\mathbf{B})^{\mathrm{T}}\mathbf{W}\mathbf{B}$, where $\mathbf{B}$ is the matrix of the velocity bases evaluated at the quadrature points and $\mathbf{W}$ is a vector of the weight and Jacobians. Secondly, the stiffness matrix is specified as the inner product of derivatives of the bases and is defined as

$$\mathbf{A} = (D_x\mathbf{B})^{\mathrm{T}}\mathbf{W}(D_x\mathbf{B}) + (D_y\mathbf{B})^{\mathrm{T}}\mathbf{W}(D_y\mathbf{B}) + (D_z\mathbf{B})^{\mathrm{T}}\mathbf{W}(D_z\mathbf{B})$$

where $D_{x,y,z}$ are the collocation derivative matrices evaluated at the quadrature points. A final matrix is defined as the inner product of a velocity base with a derivative of the pressure base and is expressed as

$$\mathscr{D}_i = (D_{x_i}\mathbf{B}_p)^{\mathrm{T}}\mathbf{W}\mathbf{B}$$

where $\mathbf{B}_p$ and $\mathbf{B}$ are the pressure and velocity base matrices, respectively. Because modal bases are used, the coefficients do not represent a physical nodal point value, thus transformations between the coefficient and physical spaces are introduced. Two transformations are defined, mapping the modal bases onto the physical space and conversely mapping a physical space onto the modal space. The backward transformation represents the summation of all modal functions with their corresponding coefficients in order to yield a physical representation of the solution at a given point distribution. This is represented by $u^{\delta}(\eta_1^{\mathrm{out}}, \eta_2^{\mathrm{out}}, \eta_3^{\mathrm{out}}) = \sum_{i=1}^{N_{\mathrm{dof}}} \hat{u}_i \phi_i(\eta_1^{\mathrm{out}}, \eta_2^{\mathrm{out}}, \eta_3^{\mathrm{out}}) = \mathbf{B}^*\hat{u}$, where $\mathbf{B}^*$ is a matrix of all the bases evaluated at specified points and $\hat{u}$ is the vector of coefficients. The backward transformation, whether used in forming matrices or in determining the physical solution, employ the sum factorization technique to reduce the operation count from $O(P^6)$ to $O(P^4)$, it is explained in Section 5.3. Conversely, the forward transformation renders a modal representation of a physical function. This operation is defined as $\hat{u} = ((\mathbf{B})^{\mathrm{T}}W\mathbf{B})^{-1}\mathbf{B}\mathbf{W}f$, where f is the physical space representation of a function evaluated at the quadrature points. This approach can be regarded as the inversion of the mass matrix represented by $\mathbf{M} = (\mathbf{B})^{\mathrm{T}}\mathbf{W}\mathbf{B}$ onto the inner product of the forcing function f and the bases.

In order to solve the Navier–Stokes equations, continuity between elements needs to be enforced. A simple case of continuity enforcement on an edge between two elements is shown in Figure 1. It is seen that in the top picture of Figure 1 the two functions do not match and thus continuity would not be enforced. On the contrary, it is seen that in the bottom picture of Figure 1 the edge functions match and continuity is enforced. Thus a requirement for continuity is that the modal bases on the boundary must match. On a face this is more complex as the local coordinates systems can have different orientations. Certainly this orientation constraint can be satisfied trivially by a special renumbering procedure, rather than a complex global solution. This renumbering scheme states that the lowest number in the element is set to the vertex D and the second lowest number is set to the vertex C while the vertices A and B are chosen such as to ensure a positive Jacobian. This ensures that the orientation of the coordinate systems matches but not necessarily the directions. Moreover, it is known that after this renumbering only certain edges and certain face modes are not continuous. Thus a sign vector is introduced to track the matching and non-matching modes. This sign vector is then used in the global assembly procedure to ensure continuity globally.

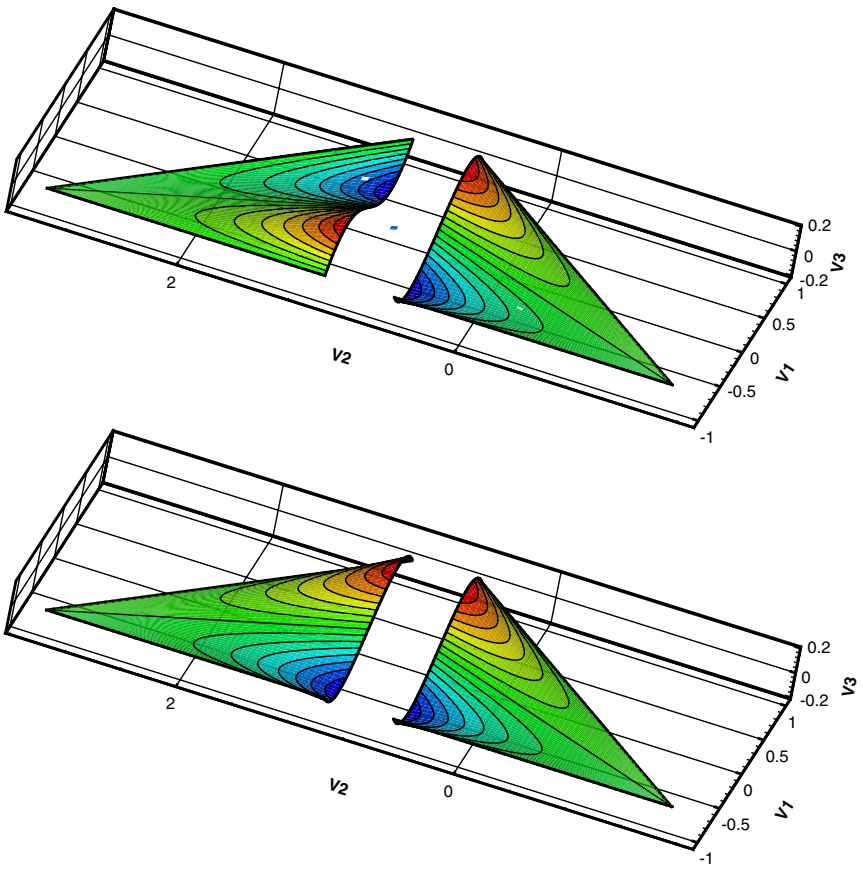

Figure 1. Continuity enforcement on an edge, representing a non-matching edge (top) and a continuous edge (bottom).

5. SPECIFIC IMPLEMENTATION DETAILS OF THE SPECTRAL ELEMENT METHOD

This section describes the specific implementation of the method developed by Sherwin and Karniadakis [15, 16], and introduces our approach. The explanations of our implementation, are included to portray different approaches in implementing the spectral element method. In addition, parallelization through the multilevel Schur complement method is explained. Finally, some challenges in the post-processing steps, needed to analyse higher order elements, are presented.

5.1. Continuity enforcement

The continuity enforcement problem is described in the previous section where a sign vector used by Sherwin and Karniadakis [15, 16] is introduced to track odd mode negations in order to enforce continuity. Ainsworth [17] developed another continuity enforcement procedure, in which the elements are collapsed onto two reference elements through a renumbering procedure. Then the elemental operations are modified, respectively, for the two reference elements, ensuring global continuity. Both of these procedures require the modification of the global assembly procedure as well as extra storage to classify the modes into groups which require special modifications and groups not requiring such modification. A modified continuity enforcement procedure is used in this study in order to reduce the complexity and memory requirement. This means that continuity is purely enforced through the local and global numbering of the vertices, which in turn guarantees continuity of the higher order functions. A vertex naming convention is shown in Figure 2, where the vertex A is defined at the collapsed coordinate $(-1,-1,-1)$, vertex B is defined at $(1,-1,-1)$, vertex C is defined at $(-1,1,-1)$ and vertex D is defined at $(-1,-1,1)$. This procedure first starts with the standard renumbering operation, which assigns the lowest global number to vertex D and the second lowest global number to vertex C. Thus matching the orientations of the collapsed coordinate systems. This procedure still leaves the problem in matching the directions of the collapsed coordinate systems. Indeed due to the construction of the collapsed coordinate system both the η_2 and η_3 directions match after the renumbering, leaving only the direction

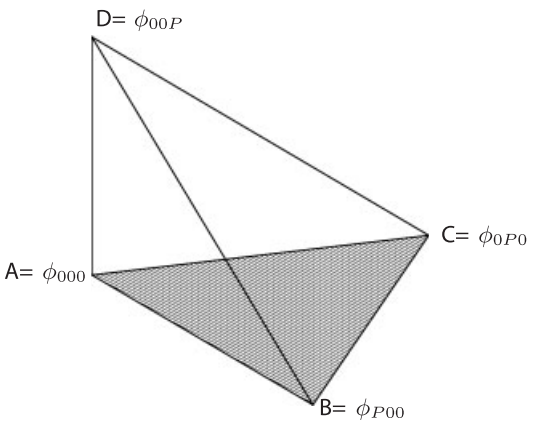

Figure 2. Vertex naming convention.

of η_1 to be matched. Note that any edge with a non-matching mode will always be shared with an AB edge. Specifically only the AB edge will have a non-matching function, while other shared edges will have matching functions. This means that by interchanging the global numbering of the A and B vertices, the direction of the η_1 coordinate is changed. In other words the final step of the continuity enforcement procedure interchanges the A and B vertices on all non-matching AB edges. Altogether this implementation enforces the continuity as a pre-processing step, just through renumbering, and does not require any modifications to the global assembly operations. The method was tested on a wide variety of meshes, and continuity was always ensured. Nevertheless, a simple continuity test, which checks if all functions match, is always performed after the pre-processing step to confirm elemental continuity.

5.2. *Reference coordinate system and curved elements*

The reference coordinate system provides a valuable analogy between the FEM and SEM. However, it is not required for the SEM as all of the elemental operations can be defined purely in the collapsed coordinate system. Thus the implementation in the current study drops the reference coordinate altogether. This means that a simple linear element in the physical coordinate system can be mapped from the collapsed coordinate system as

$$\mathbf{X}(\eta_1,\eta_2,\eta_3)=\mathbf{X_A}\phi_A(\eta_1,\eta_2,\eta_3)+\mathbf{X_B}\phi_B(\eta_1,\eta_2,\eta_3)+\mathbf{X_C}\phi_C(\eta_1,\eta_2,\eta_3)+\mathbf{X_D}\phi_D(\eta_1,\eta_2,\eta_3)$$

where $\mathbf{X}$ denotes the coordinates of the respective vertices. Moreover, the removal of the reference coordinate system simplifies the elemental operations, as they can be performed in the collapsed coordinate system and afterward mapped onto the physical coordinate system. The integration in the physical coordinate system then simplifies to

$$\int_\Omega u(x,y,z)\partial\mathbf{x}=\int_{-1}^{1}\int_{-1}^{1}\int_{-1}^{1}u(\eta_1,\eta_2,\eta_3)\left|\frac{\partial(x,y,z)}{\partial(\eta_1,\eta_2,\eta_3)}\right|\partial\eta_1\,\partial\eta_2\,\partial\eta_3$$

$$=\sum_{i}^{Q_{\mathrm{GLL}}}\sum_{j}^{Q_{\mathrm{GRL}}}\sum_{k}^{Q_{\mathrm{GRL}}}u(\eta_i^{0,0},\eta_j^{0,0},\eta_k^{0,0})\mathbf{J}_{x\to\eta}w_i^{0,0}\,w_j^{0,0}\,w_k^{0,0}$$

where the weights are now calculated with α,β constants being zero, and the Jacobian is calculated directly between the physical and collapsed coordinate system. The derivative calculation discards the mapping to the reference coordinate system and is performed on the collapsed coordinate

$$\frac{\partial u}{\partial\eta_1}=\sum_{i}^{Q}u_{pqr}^{\delta}(\eta_1^{\mathrm{GLJ}},\eta_2^{\mathrm{GRJ}},\eta_3^{\mathrm{GRJ}})\frac{\partial h_p(\eta_{1i}^{\mathrm{GLJ}})}{\partial\eta_1}\delta(\eta_{2i}^{\mathrm{GRJ}})_q\delta(\eta_{3i}^{\mathrm{GRJ}})_r=D_{\eta_1}\mathbf{B}\hat{u}$$

$$\frac{\partial u}{\partial x}=\frac{\partial u}{\partial\eta_1}\frac{\partial\eta_1}{\partial x}+\frac{\partial u}{\partial\eta_2}\frac{\partial\eta_2}{\partial x}+\frac{\partial u}{\partial\eta_3}\frac{\partial\eta_3}{\partial x}$$

where the derivatives of collapsed coordinates with respect to physical coordinate system are evaluated similar to the FEM.

Equally important, the spectral element method can represent complex geometries through expanding the mapping between the physical and collapsed coordinate systems by including

higher order modes. This is especially important for complex geometries such as in this case of pipes with two planar curvatures, and will be described briefly. By using the same expansion order as the velocity bases, the higher-order mapping is given by

$$\mathbf{X}(\eta_1, \eta_2, \eta_3) = \sum_{pqr} \hat{\mathbf{X}} \phi_{pqr}(\eta_1, \eta_2, \eta_3)$$

where $\hat{\mathbf{X}}$ is a vector of coefficients for the physical coordinate directions. Such a mapping is able to capture complex geometries, as with increasing order the number of expansion functions increases. These coefficients are determined by performing a modified local forward transformation as described by Sherwin and Karniadakis [15, 16], similar to projecting boundary conditions. Although this method permits representation of complex geometries, there exists no high order mesh generators which mesh complex geometries. Hence the geometry of the model pipe needs to be defined through a transformation function of a straight pipe, in order to capture the complexities of curvature and torsion accurately.

5.3. Derivative calculation

A different approach to derivative calculations is employed, then originally presented by Sherwin and Karniadakis [15, 16]. The original approach performs the derivative calculation in the physical space by employing Lagrange polynomials and requires the evaluation of a variable at the given quadrature points, which are also the points on which the Lagrange polynomials are defined. This evaluation is performed through backward transformation given by

$$u^{\delta}(\eta_{1i}, \eta_{2i}, \eta_{3i}) = \sum_{pqr}^{M} \hat{u}_{pqr} \phi_{pqr}(\eta_{1i}, \eta_{2i}, \eta_{3i})$$

which requires M operations for each quadrature point. However, by decomposing the basis functions into their primary functions the resulting operation count is decreased. This procedure is called tensor-product factorization and is defined as

$$u^{\delta}(\eta_{1i}, \eta_{2i}, \eta_{3i}) = \sum_{p}^{P} \sum_{q}^{P} \sum_{r}^{P} \hat{u}_{pqr} \psi_p^a(\eta_{1i}) \psi_{pq}^b(\eta_{2i}) \psi_{pqr}^c(\eta_{3i})$$

$$f_{pq}(\eta_{3i}) = \sum_{r=0}^{P} \hat{u}_{pqr} \psi_{pqr}^c(\eta_{3i})$$

$$f_p(\eta_{2i}) = \sum_{q=0}^{P} \psi_{pq}^b(\eta_{2i}) f_{pq}(\eta_{3i})$$

$$u^{\delta}(\eta_{1i}, \eta_{2i}, \eta_{3i}) = \sum_{p=0}^{P} \psi_p^a(\eta_{3i}) f_p(\eta_{3i})$$

It reduces the operation count for obtaining the physical variable at a given quadrature point distribution from $O(P^6)$ to $O(P^4)$ by performing the summation in the given steps, although it requires extra memory for two $O(P^3)$ arrays for the temporary variables f_{pq} and f_p.

Thus the original method for evaluating the derivatives in physical space using collocation differentiation is given by

$$\frac{\partial u}{\partial \eta_1}(\eta_{1i},\eta_{2j},\eta_{3k}) = \sum_{l}^{Q}\sum_{m}^{Q}\sum_{n}^{Q} \frac{\partial h_i(\eta_{1l})}{\partial \eta_1}\delta_{jm}\delta_{kn}u^{\delta}(\eta_{1l},\eta_{2m},\eta_{3n}) = \sum_{l}^{Q} \frac{\partial h_i(\eta_{1l})}{\partial \eta_1}u^{\delta}(\eta_{1l},\eta_{2j},\eta_{3k})$$

and requires $O(P^4)$ operations to obtain the derivative at the quadrature points distribution if the physical value distribution u^{δ} is known.

A different implementation is used in this study, where the derivatives of the bases are precalculated, similarly as done in the FEM. This avoids the need to perform collocation differentiation and is performed straight on the modal bases as

$$\frac{\partial u}{\partial \eta_1}(\eta_{1i},\eta_{2i},\eta_{3i}) = \sum_{pqr}^{M} \hat{u}_{pqr}\frac{\partial \phi_{pqr}}{\partial \eta_1}(\eta_{1i},\eta_{2i},\eta_{3i}) = \mathfrak{D}_{\eta_1}\hat{u}$$

where $\mathfrak{D}_{\eta_1}$ is the matrix of the derivatives of the bases evaluated at the quadrature points. Furthermore, this operation can be performed using tensor-product factorization as described previously to reduce the operation count to $O(P^4)$. The main advantage of this method is that if only the derivatives are required, they can be obtained at the expense of $O(P^4)$, compared to two $O(P^4)$ operations if collocation differentiation is used. This is because u^{δ} is needed before collocation differentiation is performed. Moreover if the derivative is just needed at one point (such as in post-processing function) or not defined on the quadrature point distribution, the precalculation method is more efficient. Although for cases where the solution and its derivatives are needed (such as in convection operator evaluations) at the quadrature point distribution, the collocation method performs these evaluations more efficiently.

5.4. *Parallelization*

Parallelization is performed by using the METIS library to perform the domain decompositions and the MPI library for communication. All of the communications employ asynchronous communication modes, thus interleaving the cost of communication with computation. This means that firstly the required operations are performed on the shared modes, and while these results are being sent, the operations on the local only modes are executed.

The parallel efficiency is increased further by using the Schur complement method to decouple the interior modes from the boundary modes. It is known that the interior modes are zero on the boundaries and are only defined in the interior. Consequently, these modes are not connected globally and are solved locally. This means that a matrix inverse operation is performed in two steps

$$(M_b - M_c M_i^{-1} M_c^{\mathrm{T}})x_b = f_b - M_c M_i^{-1} f_i$$

$$M_i x_i = f_i - M_c^{\mathrm{T}} x_b$$

where M_i is the local matrix of interior contributions, M_c is the global matrix of boundary-interior contributions and M_b is the global matrix of boundary contributions. The biggest advantage of this method is that the Cholesky decomposition of the local interior matrix M_i is stored, thus reducing the computational effort per timestep. Furthermore, all of the matrix products, such as the Schur matrix $(M_b - M_c M_i^{-1} M_c^{\mathrm{T}})$ and $M_c M_i^{-1}$ are performed locally on each parallel processor. The global matrix is only defined on the boundary modes and is

constructed through the global assembly procedure of the local Schur matrices. This global matrix is then solved using the conjugate gradient method to obtain the solution of the global boundary modes. After solving the global system the interior modes are solved locally on each processor without requiring any communication. The speedup gain is not only achieved through better parallelization but also through lower condition number of the global Schur system compared to the global matrix, resulting in less conjugate gradient iterations.

This solution strategy is improved further by performing a second level Schur complement on the boundary modes. Although the Schur complement method is expensive in terms of memory usage, current parallel computers have ample memory resources available. Thus the strategy proposes to use the available memory on parallel computers to its fullest in order to reduce the computation and communication cost of performing a matrix inverse. Furthermore, it should be mentioned that by just increasing 'virtual processors' (or threads) on each computational node, the memory requirement can be decreased, but at the same time resulting in higher communication and computation cost at each timestep.

The Schur global boundary modes are decoupled further, by noting that each parallel processor possess shared modes as well as local only modes. Note that the local only modes need not be connected globally, and can be solved locally. Firstly the global Schur complement matrix is defined as $\mathbf{S} = \mathfrak{A}^{\mathrm{T}}(M_b - M_c M_i^{-1} M_c^{\mathrm{T}})\mathfrak{A}$, where the operation $\mathfrak{A}^{\mathrm{T}} \cdots \mathfrak{A}$ represents a global assembly operation. This system is decomposed into: shared–shared contributions $\mathbf{S}_{\mathrm{SS}}$, shared–local contributions $\mathbf{S}_{\mathrm{SL}}$ and local–local contributions $\mathbf{S}_{\mathrm{LL}}$, while the global boundary modes are decomposed into local and shared contributions as $x_b = \binom{x_{b\mathrm{S}}}{x_{b\mathrm{L}}}$. This new system is solved in three steps such that

$$(\mathbf{S}_{\mathrm{SS}} - \mathbf{S}_{\mathrm{SL}}\mathbf{S}_{\mathrm{LL}}^{-1}\mathbf{S}_{\mathrm{SL}}^{\mathrm{T}})x_{b\mathrm{S}} = f_{b\mathrm{S}} - \mathbf{S}_{\mathrm{SL}}\mathbf{S}_{\mathrm{LL}}^{-1} f_{b\mathrm{L}}$$

$$\mathbf{S}_{\mathrm{LL}} x_{b\mathrm{L}} = f_{b\mathrm{L}} - \mathbf{S}_{\mathrm{SL}} x_{b\mathrm{S}}$$

$$M_i x_i = f_i - M_c^{\mathrm{T}} x_b$$

The first step represents a global solve for all of the shared modes, it is solved using a global conjugate gradient method and requires communication between processors. However, the next step corresponds to finding a solution of all the local boundary modes and is performed locally without requiring any communication. Finally, the interior modes are solved locally to complete the solution procedure. A Cholesky decomposition is performed on the local–local global Schur complement system thus reducing the computational expense per timestep. The second level Schur complement system increases the efficiency of the parallelization and decreases the computational expense of each timestep. However, the first level Schur complement system increases the efficiency only for order higher then $P = 4$ when interior modes are present, thus offsetting the higher computational effort of higher order expansions.

5.5. *Higher order post-processing*

Current state of the art spectral element visualization software displays directly the data using linear combinations of texture maps and texture shaders [18], thus representing higher order polynomials directly through pixels. Although this is a very novel and direct approach, it is not suitable for rapid implementation. Thus an implementation is developed which uses freely available visualization packages in order to achieve postprocessing capability of spectral

element data without needing advanced graphics programming skills. A similar method has been employed by Fisher [19], although on structured meshes.

The implementation used in this study fills a higher order element with linear elements, thus capturing the higher order data. Modal bases allow for the mapping of a physical solution onto any point distribution. Thus for order $p = 3$ which possesses 20 modes, 20 points are chosen and distributed at equal distances in the tetrahedron. These points are then linked to form 26 linear tetrahedrons. This simple procedure captures the higher accuracy of the method as well as curvilinear boundaries with the use of currently widely available low order visualization packages.

Although the above-mentioned procedure allows for visualizations, further postprocessing operations need to be defined in order to capture the higher accuracy of the processed data. Most of these operations require a basic procedure: finding the respective collapsed coordinate from a given physical coordinate. This operation is simple for linear elements and employs normals of the faces, however by using curvilinear elements the resulting mapping becomes complicated and an inverse function cannot be found easily. The mapping function is represented as

$$\mathbf{X}(\eta_1, \eta_2, \eta_3) = \sum_{pqr} \hat{\mathbf{X}} \phi_{pqr}(\eta_1, \eta_2, \eta_3)$$

where $\mathbf{X}$, the physical coordinate vector, is given and $\hat{\mathbf{X}}$ the modal coefficients are known. This approach requires that the collapsed coordinates η_1, η_2, η_3 are found in order to satisfy this set of three equations. In order to find a solution to these three simultaneous equations a non-linear Newton method with a constraint of $-1 \leqslant \eta \leqslant 1$ is employed. This method converges in roughly 4 iterations, although it requires the evaluation of all 9 derivatives of the mapping. Further due to the singularity of the collapsed coordinate system at the vertices C and D as well as the edge CD, derivatives at those points cannot be found. Thus the Newton method cannot be applied at those points. Vertices C and D are checked separately to avoid this problem. Moreover, on the CD edge a one-dimensional root finding algorithm in the η_3 direction is used, which does not require derivatives, in order to check if the resulting coordinate lies on the CD edge. This problem of singular points can be avoided by searching in the reference coordinate system instead of the collapsed coordinate system. By having the respective collapsed coordinate a backward transformation can be performed to obtain the physical solution at the given point. Having defined the previous procedure, the remaining post-processing functions can be determined easily. A slice is defined through a normal, which in turn is determined from the transformation function. The solution on a slice is found by simply solving the previous mapping function with an extra constraint given by the definition of a slice. To perform an integration on the slice a similar procedure is performed, although the mapping is now solved with two constraints: the definition of the slice as well as the quadrature point distribution needed. By summing all of the solutions at the quadrature points with respective weights the integral value is obtained.

6. VALIDATION

A validation study is performed on both a manufactured solution as well as the curved pipe geometry.

6.1. Validation using a manufactured solution

The Navier–Stokes equations are solved and compared with an exact solution composed of sine and cosine functions, as they are not part of our expansion bases and provide accurate convergence results. These functions are manufactured such that they satisfy the continuity equations and become

$$u = \cos(\pi x)\sin(\pi y)\sin(\pi z)\mathrm{e}^{-t}$$

$$v = \sin(\pi x)\cos(\pi y)\sin(\pi z)\mathrm{e}^{-t}$$

$$w = -2\sin(\pi x)\sin(\pi y)\cos(\pi z)\mathrm{e}^{-t}$$

$$p = -\tfrac{1}{8}[\cos(2\pi x) + \cos(2\pi y) + 4\cos(2\pi z)]\mathrm{e}^{-2t}$$

By substituting these exact solutions into the Navier–Stokes equations, the required forcing terms are found. This problem is then solved on a cube ranging from -1 to 1 with periodic boundary conditions on the cube walls. A mesh convergence study is performed such that the mesh size is decreased and the expansion order P is kept constant. This study is performed for different orders with a very small timestep of 10^{-4} in order to ensure that the time error is minimized and does not influence the convergence. Both the L_2 error norm and the H_1 error semi-norm are calculated in the coefficient space with the exact solution coefficients $\hat{u}^P$ being found through a forward transformation. The error norms are defined as

$$\varepsilon_{L_2} = \sqrt{(\hat{u}^P - \hat{u}^\delta)^{\mathrm{T}}\mathbf{M}(\hat{u}^P - \hat{u}^\delta)}$$

$$\varepsilon_{H_1} = \sqrt{(\hat{u}^P - \hat{u}^\delta)^{\mathrm{T}}\mathbf{A}(\hat{u}^P - \hat{u}^\delta)}$$

where $\mathbf{A}$ and $\mathbf{M}$ are the stiffness and mass matrices, respectively. The results for this mesh convergence studies are shown in Figure 3.

The velocity convergence rates of 3.9–4.0 for the L_2-norm and 2.5–2.6 for H_1-norm are calculated for $P = 3$ on the finest three grid points. For $P = 4$ convergence rates of 4.5–4.6 and 3.7–3.8 are found for L_2-norm, H_1-norm error norms, respectively. Furthermore, the order convergence exhibits exponential decay as expected for spectral element method.

6.2. Validation on bend pipe test case

The flow in a curved pipe is studied next to determine the validity of the code for pipe flow problems. The curved pipe is modelled by using a torus, thus not requiring periodic boundary conditions. This torus is shown in Figure 4, where the curvature ratio is defined as being the ratio of the two radii $\kappa = a/R_1$, such that a is the radius of the pipe cross-section. A pressure gradient is induced through a forcing term

$$f_x = \frac{4}{Re}\cos(\theta)$$

$$f_y = -\frac{4}{Re}\sin(\theta)$$

$$f_z = 0$$

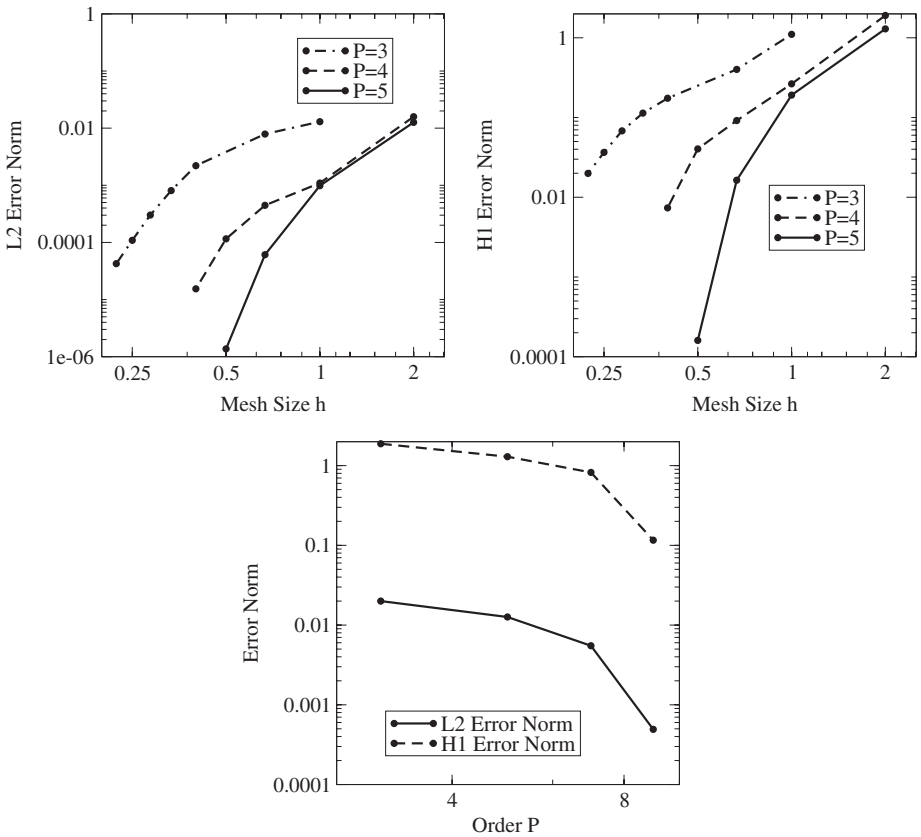

Figure 3. Mesh convergence results for the Navier–Stokes problem, L_2 error norms (left) and H_1 error semi-norm (right) and order convergence (bottom).

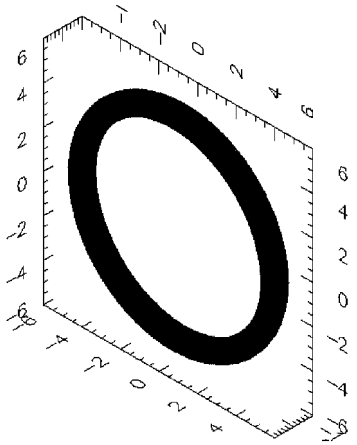

Figure 4. Torus for modelling constant curvature pipe with periodic boundary conditions.

Table I. Convergence study of friction factor ƒ.

κ	*De*	Elements	Friction factor
0.2	4.463	595	0.853
		856	0.902
		1269	0.917
		2019	0.935
		3338	0.963
		10 331	0.989
		24 613	1.0003
		38 981	1.00043
0.1	15.343	1245	0.885
		1553	0.885
		2210	0.972
		3655	0.985
		10 799	1.016
		20 304	1.032
		48 590	1.038

Table II. Comparison of friction factor ƒ values between this work and other authors.

κ	*De*	Lorrain and Bonilla [21]	Austin and Seader [22]	Yang and Chang [23]	This work
0.2	4.463		1.002	1.0006	1.00043
0.1	15.343	1.0302		1.0305	1.038

These forcing terms simulate the effect of a pressure gradient along the centreline of the pipe and allows to find the friction ratio. A friction ratio is defined as the ratio of the curved pipe flow rate to that of a straight pipe and is defined as

$$\mathrm{f} = \frac{Q_c}{Q_s} = \frac{\int_0^a \int_0^{2\pi} \mathbf{u}_c \cdot \mathbf{n} r \, \mathrm{d}r \, \mathrm{d}\theta}{\int_0^a \int_0^{2\pi} \mathbf{u}_s \cdot \mathbf{n} r \, \mathrm{d}r \, \mathrm{d}\theta}$$

A mesh convergence study on the friction factor is performed firstly, this ensures that the mesh is fine enough thus minimizing the discretization error. The mesh convergence results are presented in for third-order elements with a timestep of 10^{-3} in Table I. These friction factors compared against result, of other authors are shown in Table II for different curvature ratios as well as Dean numbers. It is seen that the values agree closely within engineering accuracy, therefore proving the validity of the code.

7. PIPES WITH TWO CURVATURES

Flows in pipes with two curvatures are studied in this section. This geometric setup allows for both the variation of curvature and torsion which represents naturally occurring pipes more accurately and has not been studied previously.

7.1. Problem description

A model pipe is constructed such that it is defined by two radii of curvature R_1 and R_2. These curvatures are present in the y–z and x–z planes, respectively. A straight pipe with cross-sectional radius of one and length of 10 is transformed into the double curved pipe by using the transformation function for the centreline

$$\tilde{x} = R_1 \cos\left(\pi\left(\frac{z-1}{9}\right)\right)$$

$$\tilde{y} = \frac{R_1}{\varepsilon}\left(\sqrt{1-\left(\varepsilon \sin\left(n * \pi\left(\frac{z-1}{9}\right)\right)\right)^2}\right)$$

$$\tilde{z} = R_1 \sin\left(\pi\left(\frac{z-1}{9}\right)\right)$$

where z is the centreline coordinate of the original straight pipe, n is the number of periods and $\varepsilon = R_1/R_2$ is the radius ratio. A constraint ($\varepsilon = (R_1/R_2) \leqslant 1$), forcing the curvature in one plane to be smaller than in the other plane, is used. This constraint prevents having a mirror geometry in the other plane. Furthermore, to ensure that the cross-sections on the centreline of the pipe are circular with the same radius, a second mapping is used such that

$$x = \tilde{x} - \frac{aby + cx}{\sqrt{1-b^2}}$$

$$y = \tilde{y} + \sqrt{1-b^2}\,y$$

$$z = \tilde{z} + \frac{ax - bcy}{\sqrt{1-b^2}}$$

where x and y are coordinates on the cross-section of the original straight pipe and a, b, c are the normalized components of the tangent centreline vector such that

$$\tilde{a} = \frac{\mathrm{d}\tilde{x}}{\mathrm{d}z} = -\frac{R_1\pi}{9}\sin\left(\pi\left(\frac{z-1}{9}\right)\right)$$

$$\tilde{b} = \frac{\mathrm{d}\tilde{y}}{\mathrm{d}z} = \frac{n\pi R_1 \varepsilon}{9}\frac{\sin\left(\pi\left(\frac{z-1}{9}\right)\right)\cos\left(\pi\left(\frac{z-1}{9}\right)\right)}{\sqrt{1-\left(\varepsilon\sin\left(n*\pi\left(\frac{z-1}{9}\right)\right)\right)^2}}$$

$$\tilde{c} = \frac{\mathrm{d}\tilde{z}}{\mathrm{d}z} = \frac{R_1\pi}{9}\cos\left(\pi\left(\frac{z-1}{9}\right)\right)$$

$$a = \frac{\tilde{a}}{\sqrt{\tilde{a}^2+\tilde{b}^2+\tilde{c}^2}}, \quad b = \frac{\tilde{b}}{\sqrt{\tilde{a}^2+\tilde{b}^2+\tilde{c}^2}}, \quad c = \frac{\tilde{c}}{\sqrt{\tilde{a}^2+\tilde{b}^2+\tilde{c}^2}}$$

An illustrative geometry is shown in Figure 5 and for a case with $n = 2$ periods a geometry is shown in Figure 6. When the radius ratio $\varepsilon = R_1/R_2$ approaches zero the transformation collapses to a simple curved pipe with a constant radius of curvature R_1.

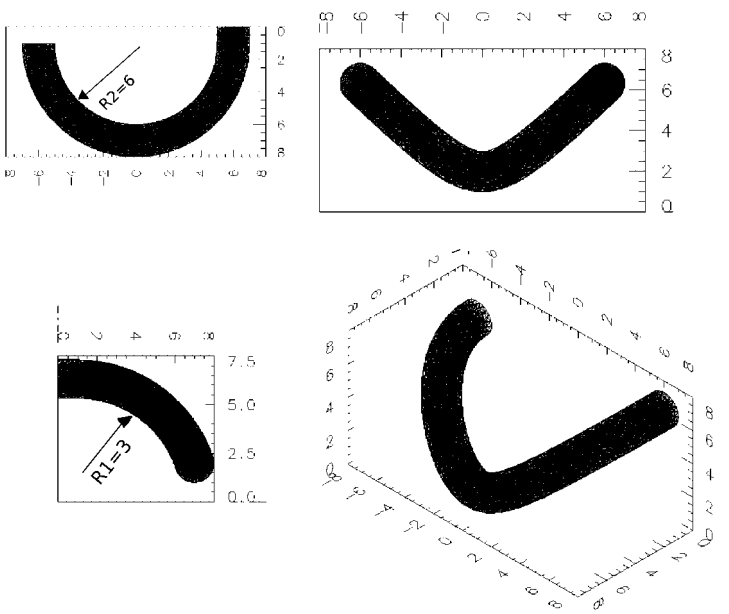

Figure 5. Pipe geometry with two curvatures defined by $R_1 = 3$ and $\varepsilon = 0.5$, top view (left top), front view (right top), left view (bottom left) and diagonal view (bottom right).

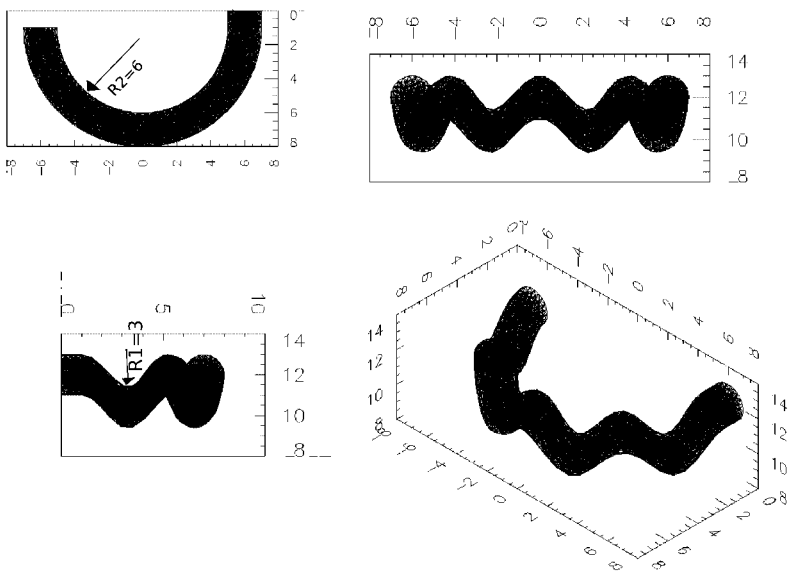

Figure 6. Pipe geometry with two periods and two curvatures defined by $R_1 = 3$ and $\varepsilon = 0.5$, top view (left top), front view (right top), left view (bottom left) and diagonal view (bottom right).

A general space curve can be fully described by its torsion and curvature, therefore these geometric properties are introduced next and the effect of transformation variables onto these properties are demonstrated. The curvature of a curve is defined as the length of the rate of change of the unit tangent vector. It measures the deviation of the curve from the tangent at each point. The curvature can be calculated from the parametric equation $r(z)$ of the centreline such that

$$\kappa = \frac{|\dot{r} \times \ddot{r}|}{|\dot{r}|^3}$$

The torsion τ is defined as the rate of change of the osculating plane of a space curve. It is calculated from the centreline equation as

$$\tau = \frac{\begin{vmatrix} \cdot & \cdot\cdot & \cdot\cdot\cdot \\ r & r & r \end{vmatrix}}{|\dot{r} \times \ddot{r}|^2}$$

These values are non-dimensionalized by the diameter of the pipe such that the curvature ratio becomes $k = \kappa D$ and the torsion ratio becomes $\Gamma = \tau D$. A pipe is uniquely defined by 3 parameters: R_1 the primary radius of curvature, ε the radius ratio and n the number of periods. The effect of these parameters on the curvature and torsion is shown in Figure 7. It is seen that with increasing primary radius of curvature R_1 the curvature decreases as expected from the inverse proportionality. Moreover, the effect of the radius ratio ε is to induce a variation of the curvature. The torsion exhibits a direct proportionality to the primary curvature radius R_1, thus increasing as the radius is increased. Nevertheless, the main contribution to the torsion is the radius ratio, which induces a change to the torsion and increases with increasing radius ratio ε. Although the effect of the period number n is expected to increase the number of changes it has a significant effect on the curvature and torsion as seen in Figure 8. It is seen that with increasing the number of periods n the curvature increases drastically with an even more pronounced effect on the torsion. Therefore, it is seen that changes to the primary radius of curvature R_1 result in mostly curvature effects, although through high radius ratios ε the

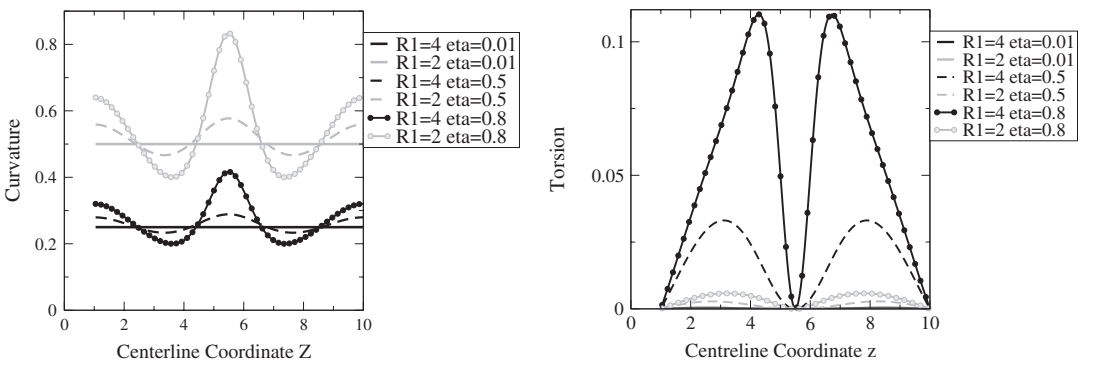

Figure 7. Effect of the primary radius of curvature R_1 and the secondary curvature ratio ε on the curvature κ (right) and torsion τ (left).

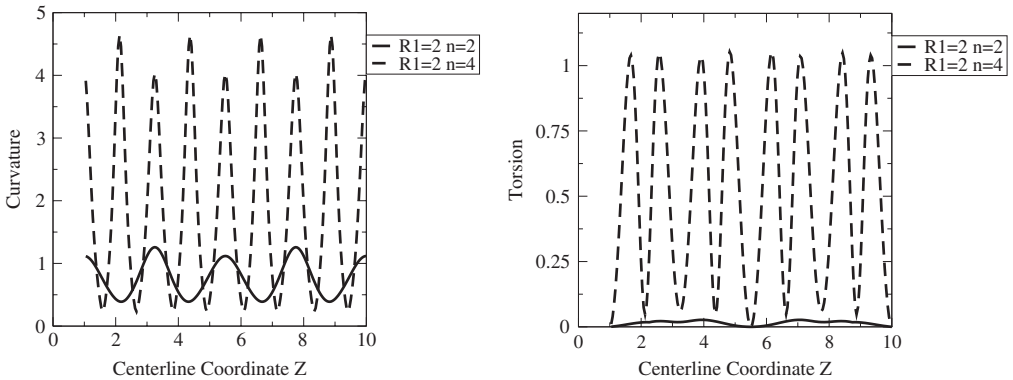

Figure 8. Effect of period number n on the curvature κ (left) and torsion τ (right) for $R_1 = 2$ and $n = 2, 4$.

Table III. Convergence study of pressure drop for double curved pipes.

R_1	ε	Elements	Pressure drop
2	0.01	503	2.7726
		2767	2.7709
		10 595	2.7728
		30 066	2.7725
	0.25	503	2.7833
		2767	2.7811
		10 595	2.7816
		30 066	2.7814
	0.5	503	2.8200
		2767	2.8172
		10 595	2.8161
		30 066	2.8159
	0.75	503	2.9040
		2767	2.9018
		10 595	2.8987
		30 066	2.8978

torsion effect can be seen. Nevertheless, the main effect of the change in torsion is seen in highly oscillatory pipes with high radius ratios and high primary radius of curvature.

7.2. *Results*

The inflow and outflow boundary conditions for the double curved pipe are set to be a parabolic velocity profile. Furthermore, the Reynolds number was set to be constant at $Re = 20$ in order to study only the geometric effects.

A mesh dependence study for the pressure drop in a double curved pipe is performed in order to assess the accuracy of the solution. These results are presented in Table III, third-order elements were used at this point with a timestep of 10^{-3}. These results demonstrate

that the effect of the mesh on the pressure drop is negligible. Furthermore, it is seen that by increasing the radius ratio ε the pressure drop increases.

Typical results obtained for the flow in double curved pipes are shown in Figure 9 as a vector field of the secondary flow, for a pipe defined by the parameters $R_1 = 4$, $\varepsilon = 0.75$ and $n = 1$. Classical Dean flow is seen in these secondary flow vector plots, however two striking differences are seen. The Dean flow is angled with respect to the horizontal line and turns. The vector pointing to the outer wall of the combined radius of curvature and the horizontal line defines this angle. Due to the periodically varying curvature, this angle changes along the centreline axis and induces the turning of the secondary flow. Consequently due to the fluid inertia and change in curvature the secondary flow does not resemble a classical Dean flow as the maximum secondary velocity is pushed towards the pipe wall. This is seen clearly at the centreline position $z = 4.0$, where the maximum centreline velocity is found near the wall and not in the centre of the pipe cross-section as in Classical Dean flows.

A more detailed analysis of the parameters affecting the secondary flow are presented in the following subsections mainly focusing on the magnitude and the angle of the secondary flow.

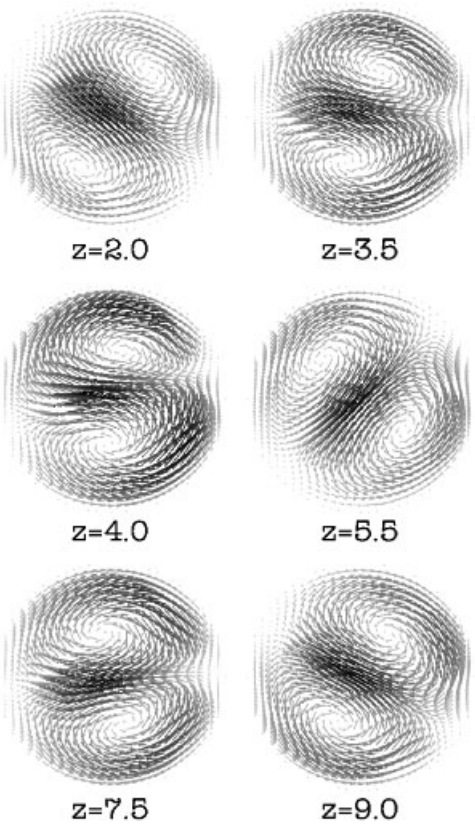

Figure 9. Secondary flow in the double curved pipe defined by $R_1 = 4$, $\varepsilon = 0.75$, $n = 1$.
Shown at given centreline positions.

7.2.1. Primary radius of curvature R_1 effect. The primary radius of curvature R_1 is mainly associated with an equivalent curved pipe. Therefore, all of the studied values are normalized with respect to a curved pipe flow. This means that the secondary velocity magnitude is normalized with the equivalent secondary velocity magnitude and represents the percentage deviation from the curved pipe solution. Furthermore, the angle is normalized with the equivalent angle of a curved pipe and represents the percentage deviation from the curved pipe solution. If the same normalization is performed on the curvature curves, the resulting normalized curvatures collapse onto one curve. These normalized values for the secondary flow magnitude at the centre and the angle of the vector along the centreline of the pipe for different R_1 values are shown in Figure 10. Note that even after normalization the curves with the same ε but different R_1 do not coincide but have different positions and values of the maximum and minimum points. These results are summarized in Table IV. Indeed it was expected that after the normalization, the effect of R_1 would be totally accounted for. However, as noted there still exists a R_1 effect as the pipe with the smaller primary radius of curvature $R_1 = 2$ has a higher velocity magnitude than the pipe with $R_1 = 4$, as well as leads by 6–8°. Lead is calculated as the equivalent angular lead of the $R_1 = 4$ curve to the $R_1 = 2$ curve. Specifically the minimum position leads by 8° while the maximum position leads by 6°. The results for the angle demonstrate a similar behaviour, although the magnitude difference is smaller than noticed for the velocity magnitude, but as before the pipe with smaller R_1 has bigger magnitude. Moreover a same leading characteristic is found, where the pipe with $R_1 = 2$ leads by 4–6°. In general, the R_1 effect of double curved pipes on the secondary velocity can

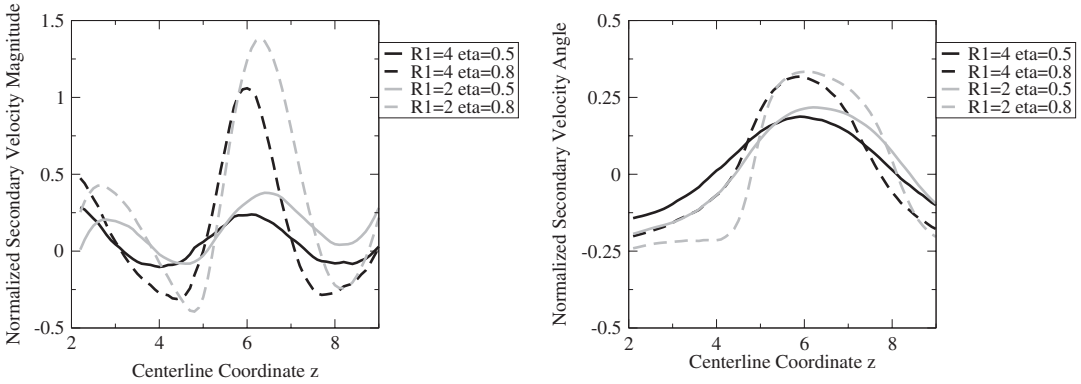

Figure 10. Effect of R_1 on the normalized secondary velocity magnitude (left) and angle (right).

Table IV. Effect of R_1 on the normalized secondary velocity magnitude and angle.

		Velocity magnitude				Angle			
R_1	ε	Min	Max	Min Lead	Max Lead	Min	Max	Min Lead	Max Lead
4	0.5	−0.0902	0.2386			−0.1428	0.1875		
4	0.8	−0.3115	1.0594			−0.2014	0.3178		
2	0.5	−0.0818	0.3793	8°	6°	−0.1937	0.2176	0°	6°
2	0.8	−0.3930	1.3821	8°	6°	−0.2407	0.3335	0°	4°

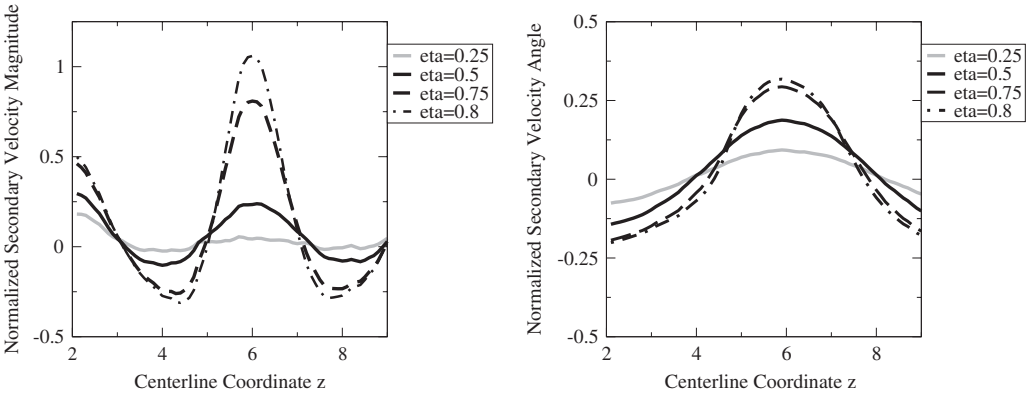

Figure 11. Effect of ε on the secondary velocity magnitude (left) and angle (right).

Table V. Curvature effect obtained through varying ε on the secondary velocity magnitude.

ε	Min Mag. as % of Min Curv.	Max Mag. as % of Max Curv.	Lead Max	Lag Min
0.25	151.983	167.550	5.4	−8.1
0.5	154.094	154.255	4.5	−0.91
0.75	153.833	158.042	5.4	−2.7
0.8	155.775	158.917	6.3	−2.7

be described as with decreasing R_1 the magnitude and the angle variation of the secondary velocity is increased while the curve is shifted right resulting in a leading curve. This effect can be explained by the inertia of the fluid as well as the torsion which was not accounted for. Firstly the geometry defined by a smaller R_1 leads to bigger curvature values, which in turn translate into more drastic geometric changes. The lead effect might be caused by the lagging response of the fluid to the geometric changes. Secondly it was noted that in pipes with two curvature, torsion is present and it has a direct relationship with R_1 as well as there is a variation of curvature. Therefore, even though the values were normalized with the curved pipe solution there is the effect of increased curvature on the magnitude of the secondary velocity.

7.2.2. Radius ratio ε effect. The effect of the primary radius of curvature was studied in the previous subsection. This subsection looks at the effect of the second curvature through the variation of the radius ratio ε while keeping the other parameters at $R_1 = 4$ and $n = 1$. Once again all of the values are normalized with respect to the curved pipe solution in order to account for the effect of primary curvature. The effect of varying the radius ratio ε on both the magnitude and angle is reported in Figure 11. It is observed that the magnitude profile resembles the curvature profile as shown in Figure 7, thus all of the results are calculated as percentage of the curvature profile to show the torsion effect. This curvature effect on the secondary velocity magnitude is summarized in Table V. It is seen that the curvature is the

Table VI. Curvature effect through varying ε on the of the secondary velocity angle.

ε	Min Angle as % of Min Curv.	Max Angle as % of Max Curv.	Max Pos.	Min Pos.
0.25	476.9	283.4	5.8	2.0
0.5	213.3	121.2	5.8	2.0
0.75	114.3	57.37	5.8	2.0
0.8	100.72	47.68	5.8	2.0

main cause of the magnitude changes with varying ε. The maximum and minimum values as percentage of the curvature values remain about constant at 153–158% with increasing ε, thus stating that the changes follow closely the changes of curvature. Similar results are obtained about the positions of the maximum and minimum values, the maximum value leads with constant value of 4.5–6.3° in relation to smaller ε geometry, while the minimum value lags by a constant value of −2.7°. However, a small secondary effect is also seen increasing this maximum and minimum values as percentages of curvature with increasing ε. This secondary effect is ascribed to the torsion effect. Moreover, the effects on the angle are summarized in Table VI. In fact these values show that there is no curvature magnitude effect on the angle, as even after the normalization the values of minimum and maximum angle as percentage of minimum and maximum values of the curvature decrease with increasing ε, while the position of these values remains constant. Therefore, this effect on the angle can be attributed to the torsion effect as curvature has been ruled out. Moreover, the leading/lagging effect once again needs to be attributed to fluid inertia as for geometries with smaller ε or change in curvature the fluid can respond quicker to the curvature change.

To conclude, the variation of ε induces both changes to curvature and torsion. These changes mainly correspond to an increased magnitude due to the curvature effect with a small secondary torsion effects as well as increased angle changed mainly influenced by the torsion.

7.2.3. Number of periods n effect. Finally, the effect of the periods is studied by varying the number of periods n while keeping the other parameters constant at $R_1 = 4$ and $\varepsilon = 0.1$. The effects on the magnitude and angle are shown in Figure 12. Previously it was observed that the number of periods not only increased the number of oscillations of curvature and torsion but also increased the amplitude of these oscillations. However, from the results presented it is seen that with increasing the number of periods both the magnitude of the normalized secondary velocity as well as angle decreases. Nevertheless, those highly oscillatory geometries are defined with rapid changes of the curvature. Thus as noticed before it is expected that the fluid inertia will reduce the response of the fluid to the geometric changes. This in turn reduces the curvature effect, which is directly linked to the secondary flow, and thus reduces with it the magnitudes of secondary velocity and angle. Where in the extreme case of $n = 6$ only wiggles are seen and not the distinctive oscillations associated with the geometric changes. Once again in order to observe effects other than the curvature, all of the values in the table are compared as percentages of the curvature values and the effect on the magnitude is summarized in Table VII. Previously it was noted that the increase in the number of periods increased both the curvature and torsion. However, it is seen that there is no curvature effect on the magnitude as with increasing number of periods there is a significant decrease in both

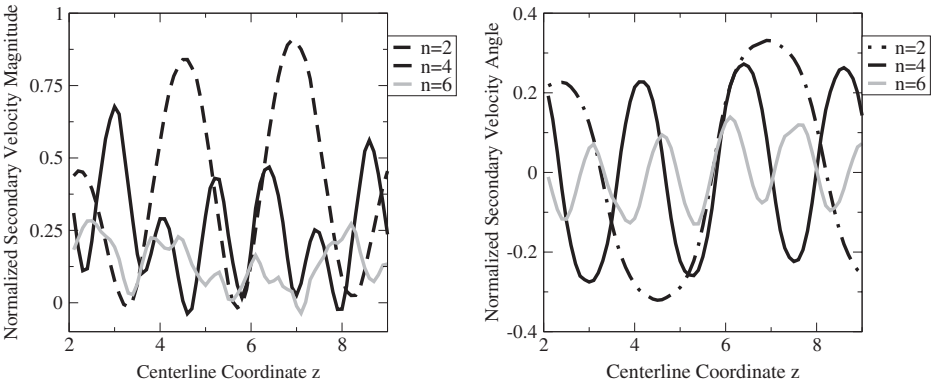

Figure 12. Effect of number of periods n on the secondary velocity magnitude (left) and angle (right).

Table VII. Curvature effect due to the number of periods n effect of the secondary velocity magnitude.

n	Min Mag as % of Min Curv.	Max Mag as % of Max Curv.
2	171.05	1166.73
4	110.81	62.8
6	43.88	9.9

Table VIII. Curvature effect due to the number of periods n effect of the secondary velocity angle.

n	Min Angle as % of Min Curv.	Max Angle as % of Max Curv.
2	3226.01	426.29
4	804.57	30.48
6	156.10	5.06

the maximum and minimum values as percentage of maximum and minimum curvature values. The effect on the angle is summarized in Table VIII. A similar result is observed as for the magnitude where with increasing number of periods the minimum and maximum angle values as percentage of the minimum and maximum curvature values decrease. This shows that the curvature effect becomes negligible with increasing number of periods, as expected from the inertia effect.

8. WALL SHEAR STRESS

A very important flow characteristic especially in blood flow is the wall shear stress. Studies by Ethier [20] have shown that the wall shear stress influences the vascular endothelial cells and can lead to atherosclerotic lesions. These lesions form in areas of very low wall shear stress. Therefore this section will study the wall shear stress on pipes with two planar curvatures,

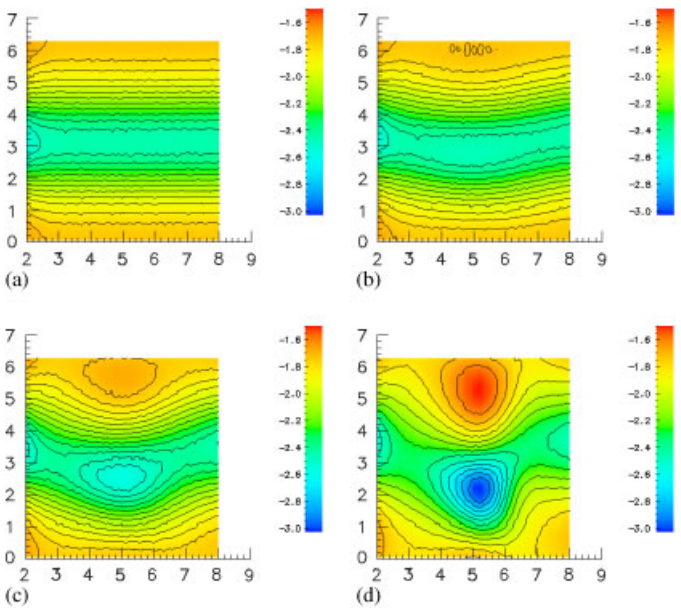

Figure 13. Effect of secondary curvature ratio for $R_1 = 4$. Wall shear stresses for pipes with $\varepsilon = 0.01$(a), 0.25(b), 0.5(c), 0.8(d).

which can be a rudimentary model for blood vessels. The wall shear stress is defined as the radial gradient of the tangential velocity component to a given pipe cross-section, and represents the frictional force onto the wall. This flow characteristic is calculated through

$$\tau_{\text{wss}} = t_1 \frac{\partial u}{\partial r} + t_2 \frac{\partial v}{\partial r} + t_3 \frac{\partial w}{\partial r}$$

where t_i are the tangential vector components. The radial derivative is calculated by introducing a new coordinate system being defined by the two normals and a tangent to a given pipe cross-section. Moreover, the tangential components are calculated from the transformation function for the double curved pipe which defines the geometry. In order to visualize the results of the wall shear stress, the pipe wall is unwound to form a rectangle. This means that the vertical axis presents the cross-sectional angle and the horizontal axis is the centreline length. The wall shear stress is calculated for different pipe configuration given by the transformation parameters R_1, ε, n, in order to determine the effect of the geometry on the wall shear stress. Firstly the results for a pipe defined by $R_1 = 4$ and $n = 1$ are shown for varying values of the secondary curvature ratio ε. These results are shown in Figure 13. It is seen from these results that the secondary curvature has a significant effect increasing both the maximum and minimum wall shear stress values. Furthermore, it is seen that by increasing the secondary curvature ratio, larger areas of low and high wall shear stress are present. Secondly, the wall shear stress is calculated for a pipe defined by $R_1 = 2$ and $n = 1$, in order to determine the primary curvature radius effect. These results are shown in Figure 14, where once again the same effect of the secondary curvature ratio is found. These results are summarized in Table IX. Furthermore

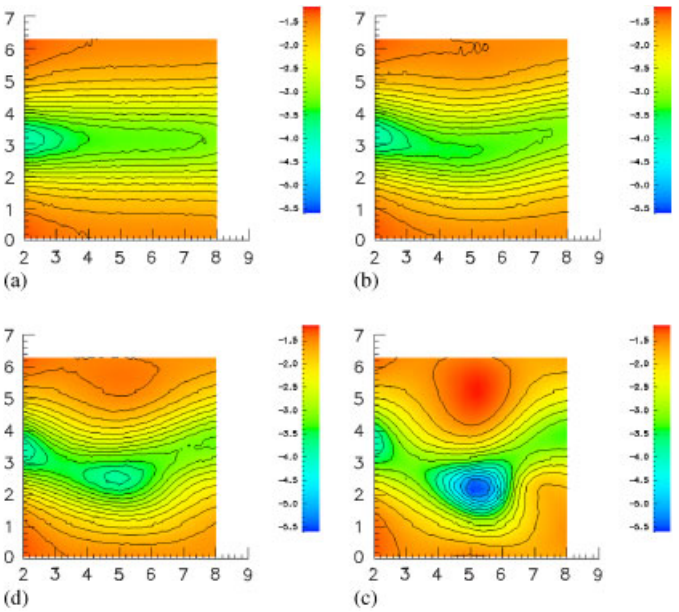

Figure 14. Effect of secondary curvature ratio for $R_1 = 2$. Wall shear stresses for pipes with $\varepsilon = 0.01$(a), 0.25(b), 0.5(c), 0.8(d).

Table IX. Effect of secondary curvature ratio ε on the wall shear stress.

	$R_1 = 4$		$R_1 = 2$	
ε	Min τ_{wss}	Max τ_{wss}	Min τ_{wss}	Max τ_{wss}
0.01	1.54	2.69	1.24	3.93
0.25	1.53	2.71	1.24	3.96
0.5	1.51	2.77	1.22	4.03
0.75	1.47	2.88	1.19	4.97
0.8	1.46	3.02	1.18	5.54

these results demonstrate that pipes with smaller R_1 have bigger variation in the wall shear stress, in addition the second curvature induced through ε produces distinct areas of wall and high shear stress.

Finally the effect of the number of periods onto the wall shear stress is studied. This means that a pipe defined by $R_1 = 4$, $\varepsilon = 0.1$ is used while the number of periods n is varied. The resulting wall shear stress is presented in Figure 15. It is seen that by increasing the number of periods the wall shear stress magnitude increases, as well as areas of low and high wall shear stress values grow larger. These results are summarized in Table X, where it is seen once again that by increasing the number of periods the magnitude of the maximum τ_{wss} increases while the minimum τ_{wss} decreases.

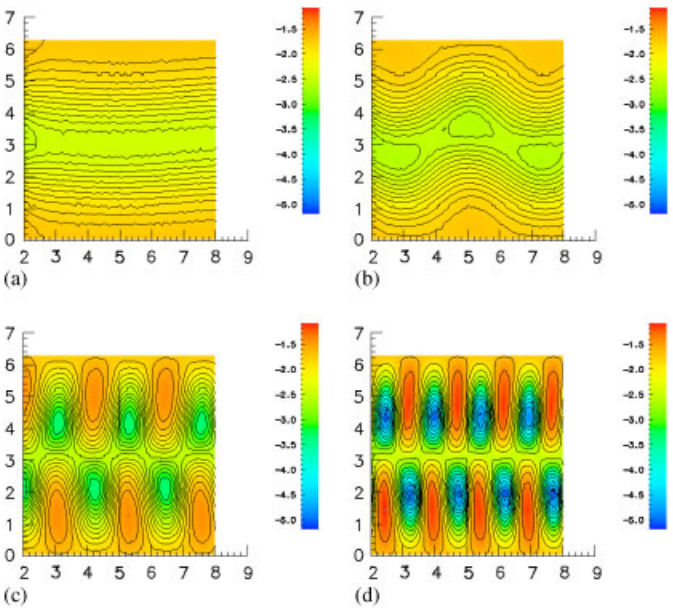

Figure 15. Effect of number of periods on a pipe with $R_1 = 2$, $\varepsilon = 0.1$. Wall shear stresses for pipes with $n = 1$(a), 2(b), 4(c), 6(d).

Table X. Effect of number of periods n on wall shear stress.

n	Min τ_{wss}	Max τ_{wss}
1	1.57	2.72
2	1.55	2.73
4	1.40	3.40
6	1.09	5.11

This section seeks to determine the underlying effect of the geometric parameters, curvature and torsion on the magnitude as well as the area of low wall shear stress. A study is performed where either the average curvature or torsion is kept constant, while the other variable is varied. Thus firstly the transformation variables R_1, ε are varied for the case of $n = 1$, such that the average curvature value is constant, while the torsion changes. These results are presented in Table XI, where the minimum and maximum wall shear stress values are listed as well as the area covered by the low wall shear stress isoline. These results show that a small increase in the torsion produces large increases in the low wall shear stress area, as well as decreases the minimum value of τ_{wss}. This is especially noticeable for high curvature values where even small torsion can have larger influence on the minimum value and low wall shear stress area. Therefore it can be said that torsion has a non-linear effect, as for values of high curvatures, very small changes in torsion produce large changes in the minimum wall

Table XI. Effect of torsion on wall shear stress τ_{wss} and area of low wall shear stress while average curvature kept same.

R_1	ε	$\bar{\kappa}$	$\bar{\tau}$	Min τ_{wss}	Area
4	0.001	0.25	0	1.70	1e−5
4.2	0.616	0.25	0.03	1.67	1.03
4.3	0.737	0.25	0.06	1.61	1.77
6.0	0.001	0.166	0	1.83	1e−5
6.2	0.509	0.166	0.15	1.81	1.13
6.4	0.701	0.166	0.40	1.76	2.00
8.0	0.01	0.125	0	1.88	1e−5
8.4	0.616	0.125	1.28	1.84	1.64
8.8	0.825	0.125	4.84	1.77	2.34

Table XII. Effect of curvature on wall shear stress τ_{wss} and area of low wall shear stress while average.

R_1	ε	$\bar{\kappa}$	$\bar{\tau}$	Min τ_{wss}	Area
4.3	0.417	0.41	0.02	1.73	0.05
4.2	0.443	0.44	0.02	1.71	0.55
4.0	0.500	0.50	0.02	1.69	1.58
6.4	0.424	0.15	0.12	1.83	0.08
6.2	0.461	0.16	0.12	1.81	0.94
6.0	0.500	0.17	0.12	1.80	1.20
8.8	0.390	0.11	0.58	1.88	1e−5
8.4	0.441	0.12	0.58	1.87	0.58
8.0	0.500	0.13	0.58	1.85	1.52

shear stress. However, for smaller values of curvature, a high change in torsion is required to obtain a similar decrease in the minimum wall shear stress.

Secondly a similar study is performed, although now the average torsion value is kept constant and the curvature value is varied. These results are presented in Table XII, where the minimum and maximum τ_{wss} values are shown as well as the area of the low shear stress isoline. These results show that with increasing curvature the minimum wall shear stress values decreases, resulting in a bigger low wall shear stress area. Moreover, it is noticed that the effect of the curvature is linear as shown in Figure 16, note that a similar change of the area as well as minimum value occurs for different torsion values if curvature is changed by a similar amount.

These results demonstrate a linear behaviour of the wall shear stress, thus decreasing the minimum τ_{wss} with increasing curvature. Recall the effect of torsion is described as non-linear. It is seen that for high values of curvature even very small amounts of torsion produced big decreases to the minimum τ_{wss}, while for smaller values of curvature much higher values of torsion are needed to produce a similar effect. In summary, it can be stated that areas of low wall shear stress will occur at points in a pipe which have both high curvature and torsion values.

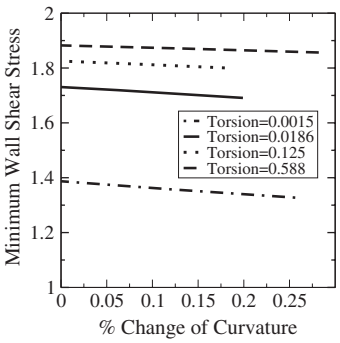

Figure 16. Effect of curvature changes onto minimum τ_{wss} when torsion is kept constant.

9. CONCLUSION

A model pipe was constructed in order to analyse both the effect of changing curvature as well as torsion. This pipe flow was solved by employing the spectral element method. The spectral element method was modified in order to simplify the continuity enforcement procedure to a preprocessing step. Further the reference coordinate system was removed and the derivatives calculated analytically. This code was validated firstly by employing a manufactured solution to the Navier–Stokes equations, and secondly by comparing with previous results obtained for a curved pipe test case. The model pipe was analysed by varying the parameters representing the geometry. It was found that even after normalizing results relative to the curved pipe solution, an effect of the primary curvature radius is observed. This effect can be attributed to the fact that changes in the primary radius of curvature no longer have a dominant effect. Other effects such as change of curvature and torsion as well as fluid inertia need to be considered. The effect of the second radius of curvature was studied by changing the radius ratio. It was found that the curvature provides the primary effect on the magnitude of the secondary centreline velocity, with a weak secondary effect governed by the torsion. However the angle was only governed by the torsion. The angle decreased by increasing the radius ratio. Moreover, it was found that the curvature effect decreases with the number of periods for both the magnitude and angle due to the fluid inertia effect. For a pipe with 6 periods, there were small amplitude oscillation which do not follow the shape of the geometry, as the fluid cannot follow the rapid geometry changes. Finally, the effect on the wall shear stress was studied. It was found that curvature has a linear effect on the wall shear stress, such that by increasing the curvature the minimum wall shear stress decreased. However, torsion exhibited a non-linear effect, where for pipes with high curvatures just small change in torsion was required to decrease the wall shear stress, while for pipes with smaller curvatures much higher change in torsion was required. Therefore, in order to avoid areas of low wall shear stress, pipes with high curvature and torsion should be avoided.

ACKNOWLEDGEMENTS

We would like to thank Natural Sciences and Engineering Research Council of Canada (NSERC) for their funding of the project as well as the Joseph Bazylewicz Fellowship for their financial support.

Further thanks go to CLUMEQ Supercomputer Center at McGill University for access to their computational resources.

REFERENCES

1. Dean WR. Note on the motion of fluid in a curved pipe. *Philosophical Magazine* 1927; **20**:208–223.
2. Berger SA, Talbot L, Yao LS. Flow in curved pipes. *Annual Review of Fluid Mechanics* 1983; **15**:461.
3. Ito H. Flow in curved pipes. *JSME International Journal* 1987; **30**:543–552.
4. Yang Z, Keller HB. Multiple laminar flows through curved pipes. *Applied Numerical Mathematics* 1986; **2**:257–271.
5. Germano M. On the effect of torsion on a helical pipe flow. *Journal of Fluid Mechanics* 1982; **125**:1–8.
6. Germano M. The Dean equations extended to a helical pipe flow. *Journal of Fluid Mechanics* 1989; **203**: 289–305.
7. Wang CY. On the low-Reynolds-number flow in a helical pipe. *Journal of Fluid Mechanics* 1981; **108**:185–194.
8. Murata S, Miyake Y, Inaba I, Ogawa H. Laminar flow in a helically coiled pipe. *Bulletin of the JSME-Japan Society of Mechanical Engineers* 1981; **24**:355–362.
9. Yamamoto K, Yanase S, Yoshida T. Torsion effect on the flow in a helical pipe. *Fluid Dynamics Research* 1994; **14**:259–273.
10. Itmoto Y, Nagata M, Yamamoto F. Steady laminar flow of viscoelastic fluid in a curved pipe of circular cross-section with varying curvature. *Journal of Non-Newtonian Fluid Mechanics* 1986; **22**:101–114.
11. Yang R, Chang SF, Wu W. Flow and heat transfer in a curved pipe with periodically varying curvature. *International Communications in Heat and Mass Transfer* 2000; **27**:133–143.
12. Cardenas Casas GA. Large eddy simulations using tetrahedral finite elements. *M.A.Sc. Thesis*, University of Toronto, 2003.
13. Bernadi C, Maday Y. *Approximations spectrales de problemes aux limites elliptiques*. Springer: Berlin, 1992.
14. Fischer PF. An overlapping Schwarz method for spectral element solution of incompressible Navier–Stokes equations. *Journal of Computational Physics* 1997; **133**:64–101.
15. Karniadakis GE, Sherwin SJ. *Spectral/hp Element Methods for CFD*. Oxford University Press: Oxford, 1999.
16. Sherwin SJ, Karniadakis GE. Tetrahedral hp finite elements: algorithms and flow simulations. *Journal of Computational Physics* 1996; **124**:14–45.
17. Ainsworth M, Coyle J. Hierarchic finite element bases on unstructured tetrahedral meshes. *International Journal for Numerical Methods in Engineering* 2003; **58**:2103–2130.
18. Peng B, Forsberg A. Directly rendering spectral elements using texture shaders. *Technical Report CS-02-17*, Brown University Computer Science Department, August 2002.
19. Fischer PF, Krause GW, Loth F. Spectral element methods for transitional flows in complex geometries. *Journal of Scientific Computing* 2002; **171**:81–98.
20. Ethier CR. Computational modeling of mass transfer and links to atherosclerosis. *Annals of Biomedical Engineering* 2002; **30**:461–471.
21. Larrain J, Bonilla CF. Theoretical analysis of pressure drop in the laminar flow of fluid in a coiled pipe. *Trans Soc Rheol* 1970; **14**:135–147.
22. Austin IR, Seader JD. Fully developed viscous flow in coiled circular pipes: *AICHE Journal* 1973; **19**:85–94.
23. Yang R, Chang SF. Numerical study of laminar flow and heat transfer in a curved pipe. *International Journal of Heat and Fluid Flow* 1993; **14**:138–145.

